

# Search for Axionlike Dark Matter Using Liquid-State Nuclear Magnetic Resonance

Julian Walter,<sup>1,2,3,\*</sup> Olympia Maliaka,<sup>1,2,3,\*</sup> Yuzhe Zhang,<sup>1,2,3,\*</sup> John Blanchard,<sup>1,2,3</sup> Gary Centers,<sup>1,2,3</sup> Arian Dogan,<sup>1,2,3</sup> Martin Engler,<sup>1,2,3</sup> Nataniel L. Figueroa,<sup>1,2,3</sup> Younggeun Kim,<sup>1,2,3</sup> Derek F. Jackson Kimball,<sup>4</sup> Matthew Lawson,<sup>5</sup> Declan W. Smith,<sup>6</sup> Alexander O. Sushkov,<sup>6,7,8,9</sup> Dmitry Budker,<sup>1,2,3,10</sup> Hendrik Bekker,<sup>1,2,3,†</sup> and Arne Wickenbrock<sup>1,2,3</sup>

<sup>1</sup>*Johannes Gutenberg-Universität Mainz, 55128 Mainz, Germany*

<sup>2</sup>*Helmholtz Institute Mainz, 55099 Mainz, Germany*

<sup>3</sup>*GSI Helmholtzzentrum für Schwerionenforschung GmbH, 64291 Darmstadt, Germany*

<sup>4</sup>*Department of Physics, California State University–East Bay, Hayward, CA 94542-3084, United States of America*

<sup>5</sup>*Physics Department, Stockholm University, Albanova University Centre, SE-10691 Stockholm, Sweden*

<sup>6</sup>*Department of Physics, Boston University, Boston, MA 02215, United States of America*

<sup>7</sup>*Department of Electrical and Computer Engineering, Boston University, Boston, MA 02215, United States of America*

<sup>8</sup>*Photonics Center, Boston University, Boston, MA 02215, United States of America*

<sup>9</sup>*Department of Physics & Astronomy, The Johns Hopkins University, Baltimore, MD 21218, United States of America*

<sup>10</sup>*Department of Physics, University of California, Berkeley, CA 94720-7300, United States of America*

We search for dark matter in the form of axionlike particles (ALPs) in the mass range  $5.576\,741\text{ neV}/c^2 - 5.577\,733\text{ neV}/c^2$  by probing their possible coupling to fermion spins through the ALP field gradient. This is achieved by performing proton nuclear magnetic resonance spectroscopy on a sample of methanol as a technical demonstration of the Cosmic Axion Spin Precession Experiment Gradient (CASPER-Gradient) Low-Field apparatus. Searching for spin-coupled ALP dark matter in this mass range with associated Compton frequencies in a 240 Hz window centered at 1.348 570 MHz resulted in a sensitivity to the ALP-proton coupling constant of  $g_{\text{ap}} \approx 3 \times 10^{-2} \text{ GeV}^{-1}$ . This narrow-bandwidth search serves as a proof-of-principle and a commissioning measurement, validating our methodology and demonstrating the experiment’s capabilities. It opens the door to probing large swaths of hitherto unexplored mass-coupling parameter space in the future by using hyperpolarized samples.

## I. INTRODUCTION

The hypothesis of dark matter (DM) is well supported by astronomical and cosmological observations. Early examples include studies of galaxy clusters by Zwicky *et al.* in the 1930s [1, 2] and of galactic rotation curves by Rubin *et al.* in the 1970s [3]. Since then, observations supporting the DM hypothesis [4–8] have been accumulating. Among various well-motivated DM candidates, axions and axionlike particles (ALPs) [9–11] are the focus of this work. These ultralight pseudoscalar bosons with possible masses between roughly  $10^{-22}$  and  $10 \text{ eV}/c^2$  [12] are introduced by theoretical models of particle physics such as string theory and grand unified theories (GUT) [13–16]. Axions are particularly of interest as they emerged as a solution to the strong- $CP$  problem of quantum chromodynamics [17, 18]. For convenience, we refer to both axions and axionlike particles as ALPs unless there is a need to distinguish them.

Considering the local DM density  $\rho_{\text{DM}} \approx 0.3 \text{ GeV}/\text{cm}^3$  [19–21] and the ALP mass, if ALPs make up a significant fraction of DM, their number density is large enough that

their collective behavior can be approximately described as a classical wave:

$$a(\mathbf{r}, t) = a_0 \cos(2\pi\nu_a t - \mathbf{k} \cdot \mathbf{r} + \phi), \quad (1)$$

where  $a_0$  is the field amplitude,  $\mathbf{r}$  is the displacement vector;  $\mathbf{k} = m_a \mathbf{v}_a / \hbar$  is the wave vector with ALP velocity  $\mathbf{v}_a$ , ALP mass  $m_a$  and the reduced Planck constant  $\hbar$ ;  $\phi$  is a random phase [22–24]. The field oscillates at a frequency close to the Compton frequency  $\nu_a = m_a c^2 / (2\pi\hbar)$ , where  $c$  is the speed of light in vacuum. Following the standard halo model (SHM) and assuming that DM is virialized in the Milky Way [25], the value of  $a_0$  can be estimated from the DM energy density  $\rho_{\text{DM}} \approx cm_a^2 a_0^2 / (2\hbar^3)$  [26]. The velocity of DM bound within the galactic halo follows a Maxwell-Boltzmann distribution with an average speed of  $v_0 \approx 220 \text{ km/s}$ , an isotropic velocity dispersion of  $v_\sigma \approx 156 \text{ km/s}$  [25], and a cut-off at the escape velocity of  $v_{\text{esc}} \approx 544 \text{ km/s}$  [27]. Taking the velocity distribution into account, a background field of axionlike DM is more accurately expressed as a sum over  $N$  independent oscillators, each of the form of Eq. (1), where the velocity of the  $n$ -th ALP is sampled from the distribution of velocities in the halo. The distribution of ALP velocities results in a spread of ALP frequencies. With a mean velocity dominated by Earth’s motion, a terrestrial detector observes the distribution of ALP frequencies with

\* These authors contributed equally to this work.

† hbekker@uni-mainz.de

a mode of  $\approx \nu_a[1 + v_0^2/(2c^2)]$  [26]. Individual ALP waves of frequency  $\nu_n$  and phase  $\phi_n$  interfere with each other and the resulting amplitude follows a Rayleigh distribution [22, 23, 28]. Therefore, the ALP field amplitude and phase vary randomly on a timescale of the characteristic coherence time  $\tau_a \approx (\nu_a v_a^2/c^2)^{-1}$  [28–30]. As it affects the computed or measured experimental sensitivity, this stochastic behavior of the ALP signal is taken into account during analysis.

There are three possible non-gravitational couplings between ALPs and Standard Model (SM) particles: (a) coupling to photons, (b) coupling to gluons and (c) coupling to fermion spins, also referred to as the gradient coupling [11]. Various experiments [31–49] search for these couplings.

The Cosmic Axion Spin Precession Experiments (CASPER), located in Boston, USA and Mainz, Germany, probe the latter two couplings to search for ALPs [26, 45, 50–53]. In this paper, we focus on measurements done with the CASPER-Gradient Low-Field (LF) apparatus, a magnetometry-based experiment that investigates the interaction between the gradient of the ALP field and atomic spins. While experiments looking for all three couplings are sensitive to stochastic fluctuations in the amplitude of the ALP field, a key distinction of experiments investigating the gradient coupling is their additional sensitivity to fluctuations in ALP velocity. The Hamiltonian of the gradient interaction can be written as:

$$H_{\text{aNN}} = g_{\text{aNN}} \nabla \mathbf{a} \cdot \mathbf{I}, \quad (2)$$

where  $g_{\text{aNN}}$  is the coupling constant and  $\mathbf{I}$  is the nuclear spin. In this paper, we focus on a measurement using a spin-1/2 proton sample. Thus, we are effectively probing the ALP gradient-proton coupling constant,  $g_{\text{ap}}$ . The magnitude of the gradient can be estimated as  $|\nabla \mathbf{a}| \approx a_0 m_a v_a / \hbar$ . The Hamiltonian in Eq. (2) is similar to that of the Zeeman interaction:  $H = -\hbar \gamma \mathbf{B} \cdot \mathbf{I}$ , where  $\gamma$  denotes the proton gyromagnetic ratio and  $\mathbf{B}$  is the applied magnetic field. In analogy to this, one can define an oscillating “pseudo-magnetic field” generated by the gradient of the ALP field

$$\mathbf{B}_{\mathbf{a}}(t) = g_{\text{ap}} \sqrt{2\hbar c \rho_{\text{DM}}} \frac{\mathbf{v}_{\mathbf{a}} \sin(2\pi \nu_a t)}{\gamma}. \quad (3)$$

To detect the presence of such a pseudo-magnetic field, we use nuclear magnetic resonance (NMR) techniques. For an ensemble of nuclear spins in a bias magnetic field  $\mathbf{B}_0$ , the Larmor frequency of the spins  $\nu_L$  is proportional to the strength of the bias field:  $\nu_L = \gamma B_0 / (2\pi)$ . If the Larmor frequency matches the Compton frequency of the ALP background, the component of the ALP-field gradient perpendicular to  $\mathbf{B}_0$ ,  $\nabla \mathbf{a}_{\perp}$ , serves as a continuous oscillating driving field, analogous to continuous-wave (cw) NMR. As with a conventional cw-NMR experiment, this results in a transverse magnetization oscillating at the Larmor frequency which could be detected using, for example, lock-in amplification.

The CASPER-Gradient-LF has a tunable magnet producing  $\mathbf{B}_0$  from zero to 0.1 T. For ALP searches in a higher mass range the CASPER-Gradient High-Field (HF) apparatus is employed with a tunable zero-to-14.1 T magnet and is in the calibration stage at the time of this work. The sensitivity of the setup is nearly frequency-independent in the range of 1 kHz to 4.3 MHz. In this work, we report on a search for the ALP-proton gradient coupling over a 240 Hz interval centered around 1.348 570 MHz ( $|\mathbf{B}_0| \approx 31.673$  31 mT). This corresponds to ALP masses in a range of 0.992 peV/ $c^2$  around  $m_a \approx 5.577$  237 neV/ $c^2$ . We use a thermally-polarized sample and focus on a narrow bandwidth to validate our methodology [50, 54] and characterize the CASPER-Gradient-LF apparatus as a tool to search for ALP DM.

## II. APPARATUS AND SAMPLE

The CASPER-Gradient-LF apparatus includes a flow-through liquid-helium cryostat containing a superconducting solenoid that can generate a bias field of up to  $B_0 = 0.1$  T. Eight superconducting shim coils surrounding the solenoid are used to reduce the field inhomogeneity to less than 2 ppm over a spherical volume with a radius of 4 mm. However, in the measurements, an inhomogeneity of approximately 10 ppm was obtained after tuning the shim fields using an algorithm based on Bayesian optimization [55]. This is larger than the 2 ppm inhomogeneity mentioned because we used a larger sample volume with a height of 22 mm and a radius of 4 mm and introduced an additional superconducting pickup coil. We chose liquid methanol ( $\text{CH}_3\text{OH}$ ) as the sample due to its high proton density (98.88 mmol/ $\text{cm}^3$ ), resulting in a total of  $7.2 \times 10^{22}$  protons, and low freezing point (175.6 K) for it to remain liquid in the cold sample holder. A variable temperature insert (VTI) is used to position the sample in the homogeneous region of the bias field. The sample is kept above the freezing point by vacuum insulation from the liquid helium and by blowing warm nitrogen gas through a spiral surrounding the sample holder. A system capable of temperature monitoring and control is currently being implemented for this work.

The sample of proton spins is thermally polarized by the bias field and acquire a net magnetization collinear to  $\mathbf{B}_0$ . To detect transverse magnetization of the sample, a niobium (Nb) pickup coil is mounted on the outside of the VTI in the liquid helium bath, see Fig. 1. The filling factor, defined as the volume ratio that the sample fills in the space enclosed by the central pickup coil, is approximately 8%. A filling factor close to unity indicates that the dimensions of the sample match those of the pickup coil, optimizing the measurement sensitivity. However, due to the necessary vacuum insulation between the pickup and the sample, it is difficult to increase the filling factor. To reduce the noise, the cryostat features a built-in superconducting Nb shield. A  $\mu$ -metal shield outside the cryogenic reservoir provides

further magnetic shielding, and the entire apparatus is itself placed within a Faraday cage.

The magnetic flux generated in the pickup coil is coupled into a direct-current Superconducting Quantum Interference Device (dc-SQUID) operated in flux-locked-loop (FLL) mode. The current in the SQUID input coil is converted into a feedback voltage, which is fed out of the cryostat and the Faraday cage via shielded copper Bayonet Neill-Concelman (BNC) cables into a Zurich Instrument MFLI Lock-in Amplifier (LIA) for processing and recording. With the excitation coils it is possible to send radio-frequency (RF) excitation pulses to conduct NMR experiments, while with the Helmholtz coils shown in Fig. 1 we can generate an offset on the bias magnetic field to scan different frequencies.

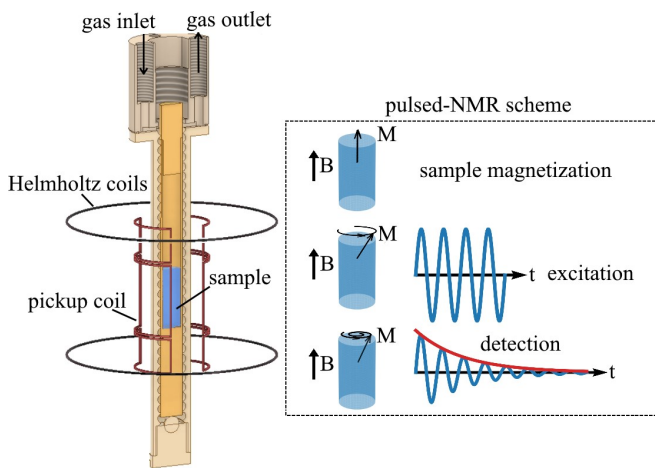


FIG. 1. Left: the sample (blue) is at the center of the pickup coil (red). The pickup coil consists of three Nb saddle-pair coils, where the area of the central coil is twice as large as the top and bottom ones. Helmholtz coils (black) are used to fine-tune the bias field. Additional saddle-pair coils (not shown) are used to apply RF-pulses. The sample temperature is regulated and kept above the freezing point by flowing nitrogen gas through the spiral surrounding the sample holder. Right: pulsed-NMR scheme, used solely for characterizing the sample: the net magnetization vector  $\mathbf{M}$  of the sample is initially along the bias field  $\mathbf{B}$ . If an excitation pulse is sent, then  $\mathbf{M}$  is tilted into the transverse plane and starts to precess. The precessing  $\mathbf{M}$  generates a signal detectable with the pickup and the SQUID.

During measurements, the SQUID and FLL electronics were battery-powered to avoid electromagnetic interference (EMI). All other electronics are outside the Faraday cage, and only cables to power the excitation and Helmholtz coils are fed through the Faraday cage. An overview of the parameters of CASPER-Gradient-LF contributing to the sensitivity is listed in Table I for this measurement and future ones.

### III. MEASUREMENT

We searched for ALPs in a range of 240 Hz centered at 1.348 570 MHz in steps of 6 Hz. The 6 Hz step size is approximately half of the NMR linewidth. At each step, the following actions were performed: 1) characterization of NMR sample and the setup, 2) dwell time of 5 s for ring-down noise to decay, 3) data collection for 100 s to search for DM over  $\approx 100$  ALP coherence times, 4) ramping the bias field to change the Larmor frequency by 6 Hz, and 5) another 5 s dwell time before repeating the steps. We performed three scans over the same frequency range to be able to cross-check potential signal candidates.

To calibrate the sensitivity of the setup and to monitor the sample temperature, a pulsed-NMR measurement was carried out at each step. In such a measurement, the magnetization vector of the sample is tilted into the transverse plane by an RF pulse creating a magnetic field perpendicular to  $\mathbf{B}_0$ . The pulse frequency is chosen close to the Larmor frequency and the pulse duration is chosen such that a tipping angle of  $\theta = \Omega_R \tau_p = \pi/2$  (usually called a  $\pi/2$ -pulse in NMR) is achieved. The Rabi frequency,  $\Omega_R$ , and the pulse duration  $\tau_p = 190 \mu\text{s}$  were found by a pulse duration sweep. The precession of the magnetization  $\mathbf{M}$  after the pulse generates an oscillating signal in the SQUID (which is maximal for a  $\pi/2$ -pulse) that decays over time. The envelope of the decay signal is indicated by the red line in the pulsed-NMR scheme in Fig. 1. The transverse magnetization of the sample decays due to homogeneous and inhomogeneous relaxation mechanisms. The homogeneous relaxation time is called  $T_2$ . The total effective relaxation time due to all mechanisms  $T_2^* \leq T_2$  can be extracted from the linewidth of the spectral line:  $T_2^* = 1/(\pi \Delta\nu)$ . Both  $T_2$  and  $T_2^*$  should be as long as possible to optimise the sensitivity in ALP searches [56].

From the feedback voltage  $V_f$  of the SQUID, the magnetic flux at the SQUID input,  $\Phi_{\text{in}}$ , as well as the magnetic flux inside the pickup coil,  $\Phi_{\text{pick}}$ , can be reconstructed [57]:

$$V_f = \frac{R_f}{M_f} \Phi_{\text{in}} = \frac{R_f}{M_f} \frac{M_{\text{in}}}{L_{\text{pick}} + L_{\text{in}}} \Phi_{\text{pick}} = \varepsilon \Phi_{\text{pick}}. \quad (4)$$

Here,  $R_f$  is the feedback resistance and  $M_f$  is the feedback-coil mutual inductance.  $L_{\text{pick}}$  and  $L_{\text{in}}$  are the inductance of the pickup coil and SQUID input coil. The flux couples into the SQUID via a mutual inductance of  $M_{\text{in}}$ . The conversion factor is  $\varepsilon \approx 0.549 \text{ mV}/\Phi_0$ , where  $\Phi_0$  denotes the magnetic flux quantum.

In the LIA, the signal is demodulated into two channels, typically called the in-phase (I) and quadrature (Q) channels. The output of the LIA,  $I + iQ$  is used to generate the power spectral density (PSD) via discrete Fast Fourier Transformation (FFT). An example of a PSD after applying a  $\pi/2$ -pulse is shown in Fig. 2 (a). A Lorentzian fit to the PSD is used to extract the Larmor frequency, the full-width-at-half-maximum (FWHM) or linewidth  $\Delta\nu$  and the power of the NMR signal. These

TABLE I. Parameters and performances of CASPER-Gradient-LF. In addition to the measurement analyzed in this paper, examples of using  $^{129}\text{Xe}$  and other samples in future measurements are considered. The polarization here refers to molar polarization, the product of polarization and concentration of the target nucleus. The polarization of methanol in this work is estimated from the proton thermal polarization at 180 K. There are numerous options for samples with polarization boosted orders of magnitude beyond thermal polarization. Here we take 180 K methanol prepolarized at 2 T and measurement time  $100 \tau_a$  as the conditions for computing the baseline of future improvements. The corresponding parameters and expected performance are listed in the third column. The xenon sample in the fourth column is  $^{129}\text{Xe}$ -enriched, and the  $^{129}\text{Xe}$  concentration can be close to unity. The details of calculations about Xe sample can be found in Ref. [26].

	This work	Examples of future CASPER-Gradient-LF	
Sample	Methanol	Methanol	Liquid $^{129}\text{Xe}$
Spin density ( $\text{cm}^{-3}$ )	$6.0 \times 10^{22}$	$6.0 \times 10^{22}$	$\sim 10^{22}$
Sample volume ( $\text{cm}^3$ )	1.2	1.2	$\sim 1$
Polarization technique	Thermal polarization	Brute Force / PHIP / DNP	SEOP
Polarization	$1.8 \times 10^{-7}$	$> 1.1 \times 10^{-5}$	$\sim 1$
$T_2$ (s)	0.71	1	1000
$B_0$ inhomogeneity (ppm)	10		$\leq 2$
Maximum scan range	1.348 450 MHz – 1.348 690 MHz 5.576 741 neV/c <sup>2</sup> – 5.577 733 neV/c <sup>2</sup>	$\sim 1$ kHz – 4.3 MHz  $\sim 4.1$ peV/c <sup>2</sup> – 17 neV/c <sup>2</sup>	$\sim 1$ kHz – 1.2 MHz  $\sim 4.1$ peV/c <sup>2</sup> – 4.9 neV/c <sup>2</sup>
Spectrum noise ( $\mu\Phi_0/\text{Hz}^{1/2}$ )	7.1		1
Spin projection noise in scan range ( $\mu\Phi_0/\text{Hz}^{1/2}$ )	0.11	8.7 at 1 kHz 0.13 at 4.3 MHz	3.5 at 1 kHz 0.11 at 1.2 MHz
$ g_{\text{aNN}} $ sensitivities in scan range ( $\text{GeV}^{-1}$ )	$3 \times 10^{-2}$	$1.0 \times 10^{-6}$ at 1 kHz $1.2 \times 10^{-5}$ at 4.3 MHz	$10^{-12}$ at 1 kHz $10^{-11}$ at 1.2 MHz

three parameters determine the setup’s sensitivity to the (pseudo)magnetic field (Eq. 3). Moreover, the sample temperature influences the linewidth. During the measurements, we did not observe significant changes in the linewidth; therefore, we conclude that the temperature was well regulated by the nitrogen gas flow.

We performed a Carr-Purcell-Meiboom-Gill (CPMG) [58] pulse sequence measurement to determine the  $T_2$  relaxation time. A  $\pi/2$ -pulse followed by a series of  $\pi$ -pulses at fixed intervals (called echo time) is sent to the sample. The resulting signal in the pickup coil features a series of spin echoes in between each two  $\pi$ -pulses (refocusing pulses). The spin-echo amplitudes decay exponentially with a decay constant  $T_2$ . We obtained  $T_2 = 0.72(5)$  s for the sample from an exponential fit to the measured spin-echo amplitudes, see Fig. 2(b). The average  $T_2^*$  time for our setup obtained from NMR-peak fits is 24.2(4.0) ms. This places our setup in the regime where the ALP-coherence time  $\tau_a = 1/(\pi\Delta\nu_a)$ , calculated from the linewidth of the ALP gradient broadening [28] at 1.348 500 MHz, is longer than  $T_2^*$ :  $\tau_a \approx 0.35$  s  $\gg T_2^*$ .

After the characterization by pulsed-NMR and the CPMG pulse sequence, a dwell time of 5 s, which is longer than the characteristic longitudinal relaxation time  $T_1$  ( $\sim 1$  s), allowed time for the sample to return close to the equilibrium magnetization. Next, we recorded  $V_f$  for 100 s without sending pulses, with the lock-in frequency detuned by 820 Hz from the initial Larmor frequency<sup>1</sup>. The sampling frequency was 13.4 kHz. The data taken in this step were analyzed for possible signatures of ALPs. To prepare for the next scan step, we increased the Larmor frequency by  $\approx 6$  Hz (half of the NMR linewidth), either by ramping the superconducting magnet or the Helmholtz coils. The scan-step size was chosen such that the resonant windows would overlap. This overlap can allow the same ALP signal to appear in several neighboring scan steps, and can be used as a validity test<sup>2</sup>. After changing the bias field there was another 5 s dwell time to ensure that the magnet power supply connection is physically interrupted in order to minimize ring-down noise in electronics. We evaluated the PSD noise level over the measurement duration and found no effects caused by the ramping process. The PSD of a full 100 s data set is plotted in Fig. 2(c).

Due to Earth’s motion, the component of the ALP gradient perpendicular to  $\mathbf{B}_0$  varies over time. This leads

to periodic modulations in signal strength, which affected the sensitivity over the duration of the measurements. We consider the most sensitive scan as the main scan, and use the other two, which we will call A and B, as consistency checks.

#### IV. DATA ANALYSIS

We analyzed the data in a way similar to that of the HAYSTAC [59], the SHAFT [60], and the CASPER-electric [52] experiments. Each 100 s time-series corresponding to one individual scan step is converted to a PSD spectrum, as shown in Fig. 2(c), which is then processed in three successive steps. First, features much narrower and wider than the expected standard halo ALP signal at the scanned frequency were smoothed out<sup>3</sup>. Subsequently, a matched filter using the ALP lineshape expected for the gradient coupling is applied to generate normalized power excess. Finally, after filtering the spectrum, bins with excess power greater than the threshold for a detection at  $5\sigma$  significance are considered as outliers. Outliers undergo a scan-rescan test to find ALP signal candidates. In the following paragraphs we describe these analysis steps in detail.

Savitzky-Golay (SG) filters [64] are commonly used to smooth out features of a spectrum that are either narrower or wider than the expected signal. In the spectra, noise spikes can appear, for example, due to EMI penetrating the shields. Additionally, impedance mismatch in the detection chain, composed of the pickup coil, the SQUID and the LIA, can lead to a broad and uneven baseline. We chose one half of the expected ALP linewidth at the scanned frequency as the filter window and applied a second-order SG filter to smooth out any features narrower than this. If narrow features are present on top of an ALP signal, the signal lineshape can appear significantly distorted in the filter response, as we found by injecting simulated ALP signals into the data. To minimize distortion, we refined the smoothing to selectively address only those narrow features that are unlikely to stem from white noise: the SG-filter response was subtracted from the unfiltered spectrum, leaving a residual spectrum containing only features narrower than the filter window. The values in the (residual) PSD are expected to stem from a  $\chi^2$  distribution with two degrees of freedom, if the time-series signals from the in-phase and quadrature channels of the LIA contain just Gaussian-distributed noise. We performed  $\chi^2$  fits to the histograms of the residual PSD, and determined the

<sup>1</sup> We detuned the lock-in frequency from the Larmor frequency by a few hundred hertz. Such a non-zero difference frequency presents a number of advantages. For example, the demodulated signal oscillates at the difference frequency which, being a signature of the NMR signal, can be easily distinguished from noise.

<sup>2</sup> The strength of an ALP signal detected in multiple scan steps depends on the detunings of Larmor frequencies from the ALP Compton frequency. Such variation of ALP signal strength can be used to test the ALP signal candidates.

<sup>3</sup> This step renders the analysis insensitive to scenarios other than the standard halo model. For example, some models predict the existence of fine-grained DM streams in the galaxy [61–63]. Such streams would feature a small velocity dispersion and would thus have spectral signatures narrower than what we consider in this work.

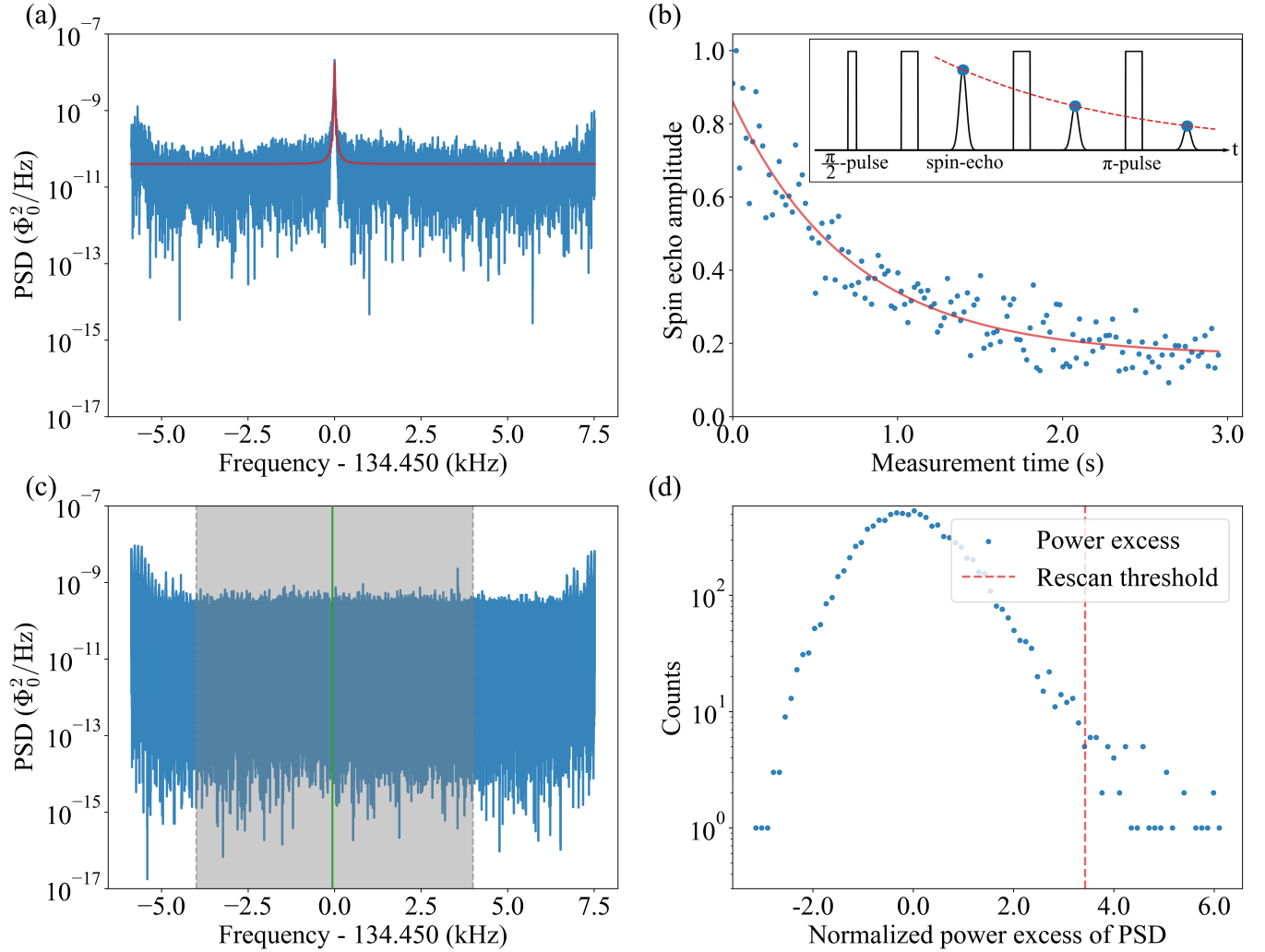


FIG. 2. **(a)** PSD generated from the time-series of  $\Phi_{\text{in}}$  after a  $\pi/2$ -pulse. The NMR peak was fitted with a Lorentzian function (red line). The center of the peak is at 1348449.21(5) Hz with a FWHM of 14.79(1) Hz. **(b)** CPMG-pulse-sequence measurement taken prior to the ALP-search steps. From an exponential fit (red line)  $y(t) = Ae^{-t/T_2} + B$ , where  $t$  is time and  $y(t)$  is the normalized spin-echo amplitude (indicated by the blue dots), the relaxation time is extracted as  $T_2 = 0.72(5)$  s. **(c)** PSD of the first 100 s ALP-search step. Structures at the lower and upper edges of the spectrum are artifacts from compensating for the built-in band pass filter of the LIA. The analysis window (grey) is centered at the Larmor frequency and has a width of 8 kHz to exclude the filter artifacts at the edges. Parts of the spectrum outside of this window are not used in the data analysis. We compute the noise baseline of each PSD within the analysis window. For the spectrum shown, the average noise level is  $3.97(6) \times 10^{-11} \Phi_0^2/\text{Hz}$ . We chose a resonant window (green)  $\pm 5$  NMR linewidths ( $\pm 70$  Hz) around the Larmor frequency to search for ALP-signal candidates around the Larmor frequency. ALP candidates found outside the resonant window, can be used to disqualify candidates found on resonance in other data sets. **(d)** Histogram of the normalized power excess (NPE) generated from the PSD in (c) with the rescan threshold (red line) at the 95% confidence limit for a  $5\sigma$ -ALP detection.

threshold for outliers. In the raw spectrum, if some PSD values differed from the filter response by an amount exceeding this threshold, they were identified as non-white-noise spikes. Only these PSD bins as well as their four nearest neighbors were substituted with the average of the SG filter window, smoothing out those spikes that are likely EMI while preserving potential ALP signals. We refer to the spectra after undergoing this spike suppression guided by SG-filter residuals as the spike-corrected spectra. In all spike-corrected spectra of the main scan, 0.002% of the total data points were modified in this way; in rescan A and B, 0.004% and 0.003% of points were modified.

Next, we performed a reduced chi-square test on the filtered spectrum to verify if the remaining noise is of purely random nature. The test indicates the presence of a noise floor (baseline) that is not flat over the analysis window. To characterize the remaining noise, we fitted the spectrum baseline by applying another broad SG filter, this time with a filter window length of 200 ALP linewidths. For normalization, this noise baseline is subtracted from the spike-corrected spectrum, then the result is divided by the baseline. An estimation of analysis efficiency considering all filtering steps is presented at the end of this section and is derived in more detail in the Appe.

To search for ALP signal candidates in the spectra after baseline removal, we applied a matched filter (also known as optimal filter) using the expected ALP signal lineshape. For each scan step, we determined the spectral lineshape  $\lambda(\nu, \nu_a)$  of the ALP signal as a function of frequency  $\nu$  and ALP Compton frequency  $\nu_a$ . The lineshape also depends on the continuously changing orientation of the sensitive axis of the setup with respect to the direction of Earth's motion through the DM halo [28]. Matched filtering is performed by convolving the PSD with the lineshape at a series of ALP Compton frequencies in the analysis window. The step size of the matched filter was chosen to be half the ALP linewidth. As verified empirically, such a step size not only maximizes the signal-to-noise ratio (SNR) but also reduces the analysis time compared to finer step sizes. The result of matched filtering, normalized by its standard deviation, is referred to as normalized power excess (NPE).

To assess the likelihood of an ALP signal being present in the NPE, we conducted a hypothesis test using the NPE of each scan step as a test statistic. Here we defined the presence of an ALP signal as the null hypothesis, and the absence of it as the alternative hypothesis. We modeled the NPE at the ALP frequency bin for the two scenarios of a signal at  $5\sigma$  significance being present, and not being present, by performing Monte-Carlo (MC) simulations (see Section C 1 in the Appendix for details). From the cumulative distribution functions (CDFs) obtained for both cases we located the NPE value  $\Theta_{\text{RE}}$  corresponding to the left-tail 95% confidence interval limit of the null hypothesis, yielding a p-value of 0.001. A histogram of the NPE is calculated with a bin width chosen

according to the Freedman-Diaconis rule [65] to balance data resolution and noise, as shown in Fig. 2 (d). In the NPE spectra, frequency bins at which the NPE value exceeds  $\Theta_{\text{RE}}$  were considered outliers, which were then tested against the data sets of scans A and B to determine whether they could be ALP signal candidates.

	Main scan	Scan A	Scan B
$N$	481 680	481 680	481 680
$\langle X \rangle$	145 (0.03%)	145 (0.03%)	145 (0.03%)
$X$	6393 (1.32%)	5760 (1.20%)	6202 (1.29%)
$X'$	5	7	3
$X''$	5	5	3
$X'''$	-	0	0

TABLE II. Results of the three ALP scans.  $N$ : number of bins in all NPE spectra.  $\langle X \rangle$ : statistically expected number of outliers, assuming only white noise.  $X$ : number of outliers (bins above rescan threshold).  $X'$ : number of ALP signal candidates (outliers within resonant windows).  $X''$ : number of candidates after merging (candidates closer than one ALP linewidth are merged).  $X'''$ : number of candidates appearing in this scan and also in the main scan within four ALP linewidths.

Table II lists the outliers and ALP signal candidates discovered over the investigated frequency range. At every scan step the number of outliers,  $X$ , exceeds the statistically expected number of false positives,  $\langle X \rangle$ , by at least an order of magnitude ( $X \geq 10\langle X \rangle$ ). The excess outliers in each spectrum were found to stem from non-white noise with linewidths neither narrow nor broad enough to be smoothed out by the SG filters. By distinguishing between resonant regions and backgrounds in the spectra, and by comparing the main scan to the rescans, we identified outliers resulting from noise.

Our setup is only sensitive to ALP interactions when the Larmor frequency of the sample spins is near the ALP Compton frequency. For that reason, out of the total number of outliers,  $X$ , we considered only the  $X'$  outliers within the resonant window to be candidates in need of further inspection. In each scan step, candidates appearing less than one ALP linewidth apart (approximately 1 Hz) were considered as a single candidate. This process reduced the number of candidates to  $X''$ . The next step was to check whether any candidate in the main scan appeared in the other two scans as well. No such candidates were found; therefore, we conclude that no ALP gradient interaction was discovered at the detection sensitivity.

In the absence of ALP-signal detection at the  $5\sigma$  level, we calculate an upper limit for  $g_{\text{ap}}$ :

$$|g_{\text{ap, lim}}| = \sqrt{\frac{e_5}{\eta P_{\perp, 1}}}. \quad (5)$$

Here,  $e_5$  denotes the signal power corresponding to the  $5\sigma$  threshold of the NPE distribution.  $P_{\perp,1}$  is a reference signal power expected for the case  $|g_{\text{ap}}| = 1 \text{ GeV}^{-1}$ . It is essential to correct the setup sensitivity and the coupling constants of ALP signal candidates for the efficiency of signal recovery,  $\eta$ . We defined the efficiency of the analysis as the ratio of signal power recovered by the analysis to its original value, and we obtained with MC simulations  $\eta = 88.2(4.6)\%$  (see Section C 1).

The limits obtained from our proof-of-concept measurements are plotted in Fig. 3.

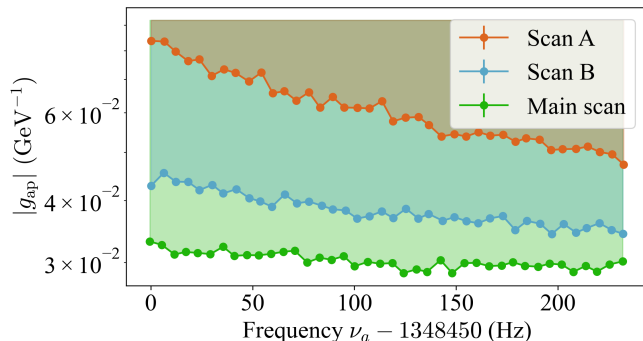


FIG. 3. ALP gradient-proton couplings excluded at the 95% confidence level by the three sequential scans. Each data point represents the sensitivity to an ALP signal on resonance with the Larmor frequency of the respective scan step. Data taking happened within a time of approximately six hours, therefore the daily modulation of the ALP signal amplitude lead to an increase in sensitivity (see Fig. 6 in the Appendix).

## V. CONCLUSIONS AND OUTLOOK

We present an experimental search for galactic dark matter ALPs interacting with the protons of a thermally-polarized methanol sample employing SQUID-based detection of the transverse magnetization. This is the first dedicated laboratory search in this general mass range. We scanned from  $5.576741 \text{ neV}/c^2$  to  $5.577733 \text{ neV}/c^2$  corresponding to a Compton frequency range of 240 Hz ( $\approx 200$  ALP linewidths) centered at 1.348570 MHz. We find no statistically significant evidence of ALP dark matter signals after performing a set of consistency checks. This sets the ALP gradient-proton coupling  $|g_{\text{ap}}| \leq 3 \times 10^{-2} \text{ GeV}^{-1}$  as the constraint in the scanned ALP mass range. This narrow-bandwidth search serves as a commissioning test, and proof of principle for the methodology of CASPER-Gradient-LF.

In ongoing experimental efforts, we employ various samples of higher nuclear-spin polarization. Those samples are polarized by techniques such as prepolarization in a strong magnetic field and low temperature (also referred to as “Brute Force”), spin exchange optical pumping (SEOP), parahydrogen induced polarization (PHIP)

and dynamic nuclear polarization (DNP) [66]. The polarization could reach the order of unity at maximum, boosting the sensitivity by more than six orders of magnitude compared to thermal polarization in this work.

More methods are being developed to improve the sensitivity by up to four orders of magnitude, such as prolonging the relaxation time  $T_2$  and increasing bias-field homogeneity. Examples of using hyperpolarized samples with long relaxation times are given in the Table I. Increasing the volume of the sample can further improve the sensitivity. The flexibility in the choice of sample is also advantageous to distinguish between various axion and ALP models that can have different couplings to protons and neutrons [67]. With these upgrades, CASPER-Gradient-LF is expected to probe the previously unexplored well-motivated ALP parameter space.

## ACKNOWLEDGMENTS

The authors acknowledge helpful discussions with Pablo Chrisvert, Jiawei Gao, Daniel Gavilan Martin, Grzegorz Lukaszewicz, Ophir Ruimi, Malavika Unni, and Pengyu Zhou. This work was supported in part by the Cluster of Excellence “Precision Physics, Fundamental Interactions, and Structure of Matter” (PRISMA+ EXC 2118/1) funded by the German Research Foundation (DFG) within the German Excellence Strategy (Project ID 39083149) and COST Action COSMIC WIS-Pers CA21106, supported by COST (European Cooperation in Science and Technology), and also by the U.S. National Science Foundation under grant PHYS-2110388. The work of Y. Kim was supported by the Alexander von Humboldt Foundation. The work of A.O.S. was supported by the U.S. National Science Foundation CAREER Grant No. PHY-2145162, the U.S. Department of Energy, Office of High Energy Physics under the QuantISED program, FWP 100667, and by the Gordon and Betty Moore Foundation, grant DOI 10.37807/gbmf12248.

## Appendix A: Detection chain properties

The properties of the dc-SQUID sensor used for this measurement are listed in Table III. The magnetic flux coupled into the SQUID,  $\Phi_{\text{in}}$ , can be obtained from the feedback voltage signal,  $V_f$ , via the relation:

$$\Phi_{\text{in}} = \frac{M_f}{R_f} V_f, \quad (\text{A1})$$

where  $M_f$  is the feedback-coil inductance and  $R_f$  is the feedback resistance. Figure 4 shows the full PSD spec-

TABLE III. Properties of SQUID sensor in use. Note that  $R_f$  can be set to different values.

Pickup coil inductance ( $L_{\text{pick}}$ )	553 nH
SQUID input coil inductance ( $L_{\text{in}}$ )	400 nH
Mutual inductance ( $M_{\text{in}}$ )	3.98 nH
Feedback-coil inductance ( $M_f$ )	$22.83 \Phi_0/\text{mA}$
Feedback resistance ( $R_f$ )	3 k $\Omega$

trum of the SQUID with the bias magnetic field turned off and without sample.

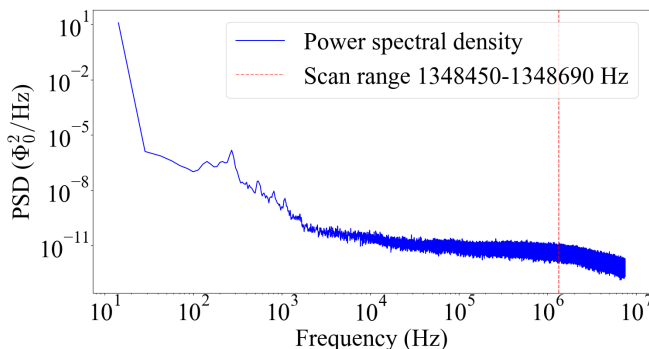


FIG. 4. Spectrum showing the bandwidth of the SQUID, recorded with the bias field off and without sample. The frequency probed in this work is marked by a dotted red line. The shown spectrum is an average of 10 spectra.

We characterize the detection chain with the transfer coefficient  $\beta$ , which defines the relation between sample magnetization perpendicular to the bias field,  $M_{\perp}$ , and the amplitude of the oscillating feedback voltage of the SQUID,  $V_{\perp}$ :

$$\beta = \frac{V_{\perp}}{\mu_0 M_{\perp}}, \quad (\text{A2})$$

with the vacuum magnetic permeability,  $\mu_0$ . In the special case of  $\pi/2$ -pulsing, the sample magnetization vector is tilted into the transverse plane and  $M_{\perp} =$

$M_0 \sin(\pi/2) = M_0$  holds, where  $M_0$  is the equilibrium magnetization of the sample. For each scan step, we measured the feedback-voltage amplitude right after such a pulse,  $V_0$ , and calculated the equilibrium magnetization of the liquid methanol sample [68]:

$$M_0 = \frac{n\gamma^2 \hbar^2 I(I+1) B_0}{3k_B T}. \quad (\text{A3})$$

Here,  $\hbar$  is the reduced Planck constant,  $k_B$  is the Boltzmann constant,  $n$  is the number density of protons and  $I$  is the nuclear spin. The proton is a spin 1/2 particle with a gyromagnetic ratio of  $\gamma = 2\pi \times 42.577$  MHz/T. With four protons per methanol molecule, the sample contained  $7.2 \times 10^{22}$  protons within a cylindrical volume of  $1.2 \text{ cm}^3$ , with 4 mm radius and 24 mm height. The sample at a temperature  $T \approx 180$  K was placed within a bias field  $B_0$  varying over the scans. At a bias field of  $B_0 = 0.0317$  T we find an equilibrium magnetization of  $M_0 \approx 1.86 \times 10^{-10} \text{ T}/\mu_0$ . We computed the SQUID transfer coefficients for all scan steps and found an average value of  $\beta \approx 4 \times 10^6 \text{ V/T}$ .

## Appendix B: Expected axionlike-particle signal

The magnetometer responds to the gradient of the ALP field,  $\nabla a$ , which can be treated as a pseudo-magnetic field. The response has a linear dependence on  $\nabla a_{\perp}$ , the component of  $\nabla a$  perpendicular to the bias field. In the measurements analyzed in this work, the NMR linewidth is ten times broader than the expected ALP linewidth, therefore the ALP-induced signal follows the spectral lineshape of  $\nabla a_{\perp}$  [56]. The PSD of the signal is given by:

$$|S_{\perp}(\nu, \nu_a)|^2 = P_{\perp} \lambda_{\perp}(\nu, \nu_a), \quad (\text{B1})$$

where  $\nu$  is the frequency,  $\nu_a$  is the ALP Compton frequency,  $P_{\perp}$  is time-averaged signal power and  $\lambda_{\perp}(\nu, \nu_a)$  is the normalized averaged spectral lineshape of  $\nabla a_{\perp}$  as found in Eq. (22) of Ref. [28].  $\lambda_{\perp}(\nu, \nu_a)$  is illustrated in Fig. 5. In this work, we present PSDs in the units of  $\Phi_0^2/\text{Hz}$ , where  $\Phi_0$  is the magnetic flux quantum.  $P_{\perp}$  can be derived as [52]:

$$\begin{aligned} P_{\perp} &= \frac{1}{2} \left( \frac{M_f}{R_f} \beta \mu_0 M_0 u \right)^2 \langle \xi^2 \rangle \\ &= \frac{1}{2} (\Phi_{\pi/2} u)^2 \langle \xi^2 \rangle. \end{aligned} \quad (\text{B2})$$

Here,  $\Phi_{\pi/2}$  refers to the magnetic flux in the SQUID after a  $\pi/2$ -pulse, converted from the feedback voltage by Eqs. (A1) and (A2). The spectral factor  $u$ , which is a function of Larmor frequency  $\nu_L$ , can be regarded as the effective fraction of on-resonance spins.  $\xi$  is the tipping angle. In the following, we expand on the parameters in Eq. (B2).

The ALP-field gradient transverse to the bias field (acting as an oscillating pseudo-magnetic field) would

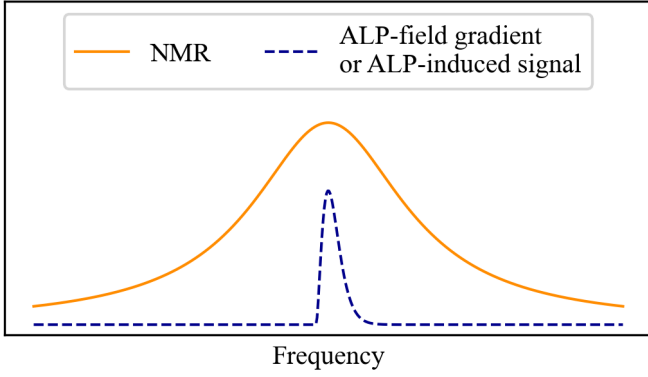


FIG. 5. Illustration of spectral lineshapes of NMR, the ALP-field gradient and the ALP-induced signal. In the shown scenario, where the NMR linewidth is much broader than the ALP-field gradient, only a small fraction of the spins are on-resonance, and the signal lineshape follows the ALP-field gradient.

slightly tip the sample magnetization from its equilibrium orientation. The root-mean-squared (rms) tipping angle is determined by the rms Rabi frequency  $\Omega_a$ , relaxation time  $T_2$  and the ALP-coherence time  $\tau_a$  [56]:

$$\sqrt{\langle \xi^2 \rangle} \approx \Omega_a T_2 \sqrt{\frac{\tau_a}{\tau_a + T_2}} = \begin{cases} \Omega_a \sqrt{\tau_a T_2}, & \tau_a \ll T_2 \\ \Omega_a T_2, & T_2 \ll \tau_a \end{cases}. \quad (\text{B3})$$

Note that as an implication of the stochastic nature of the ALP field, the Rabi frequency is not constant; therefore we use its rms value [30]:

$$\Omega_a \approx \frac{1}{2} \frac{c}{\hbar} g_{\text{aNN}} a_0 m_a v_{\perp} = \frac{1}{2} g_{\text{aNN}} \sqrt{2\hbar c \rho_{DM}} v_{\perp}, \quad (\text{B4})$$

with the speed of light  $c$ , the gradient coupling constant  $g_{\text{aNN}}$ , the rms ALP-field amplitude  $a_0$  and the ALP mass  $m_a = \nu_a (2\pi\hbar/c^2)$ .  $v_{\perp} = v_a \sin \alpha$  refers to the magnitude of the ALP velocity perpendicular to  $\mathbf{B}_0$ , where  $\alpha$  is the angle between the ALP velocity,  $\mathbf{v}_a$ , and  $\mathbf{B}_0$  (refer to Fig. 1 of Ref. [28]).  $v_a$  is boosted by the velocity of the terrestrial detector relative to the galactic rest frame. This velocity is dominated by the galactic rotation speed at the solar radius,  $v_{\odot} \approx 233$  km/s. Earth's motion introduces annual and daily modulation into  $v_{\perp}$ . During the six-hour measurement,  $v_{\perp} = v_a \sin \alpha$  varied by around 50% due to the daily modulation of  $\alpha$ , which is plotted in Fig. 6. Meanwhile, the magnitude of  $v_a$  varied by less than 1% around  $v_{\odot}$  over the measurement duration. The factor of 1/2 in Eq. (B4) arises because only one of the two counter-rotating components of the linearly-polarized drive field is on resonance (rotating-wave approximation).

In the spectral factor  $u$ , we consider the fraction of spins on-resonance with the ALP-field gradient. Considering the linewidth of NMR ( $\Delta\nu_{\text{NMR}}/\nu \approx 10$  ppm) and the ALP-field gradient ( $\Delta\nu_a/\nu \approx 1$  ppm), we can roughly

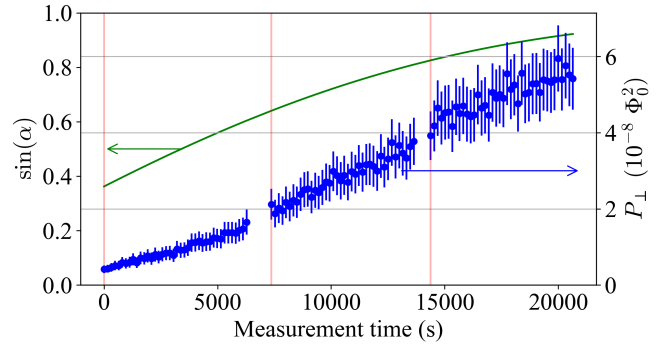


FIG. 6. ALP parameters modulated by Earth's motion. Plotted for the start times of each measurement step for each of the three scans in seconds. Zero time corresponds to start of the data taking on December 23, 2022, 15:47:30 (Central European Time, UTC+1). Vertical dashed red lines mark the beginning time of a scan. Green line:  $\sin(\alpha)$  oscillates with a period of one day. Blue dot with error bar: expected ALP signal powers in the PSD, according to Eq. (B2), for the reference case of an ALP gradient coupling to proton of  $g_{\text{ap}} = 1 \text{ GeV}^{-1}$ . Uncertainties for these values were propagated from errors of the spin relaxation times  $T_2$  and  $T_2^*$ , sample Larmor frequency  $\nu_L$  and NMR signal power  $P_{\text{NMR}}$ .

estimate the spectral factor to be  $u \approx 10\%$ . A more precise value can be computed by:

$$u = \frac{\Delta\nu_a}{\Delta\nu_{\text{NMR}}} = \frac{T_2^*}{\tau_a}. \quad (\text{B5})$$

For the measurements around 1.348 500 MHz, with  $T_2^* = 24.2(4.0)$  ms and  $\tau_a \approx 0.35$  s, the spectral factor  $u$  is approximately 7%.

Summarizing the above contributions, we arrive at the expected rms ALP-signal amplitude:

$$|S_{\perp}(\nu, \nu_a)|_{\text{rms}}^2 = \frac{1}{2} [\Phi_{\pi/2} u \Omega_a T_2]^2 \frac{\tau_a}{\tau_a + T_2} \lambda_{\perp}(\nu, \nu_a). \quad (\text{B6})$$

We used synthetic ALP signals to test the recovery of signal candidate coupling constants, and to derive the sensitivity of the measurement, see section C 1. Such signals were generated by evaluating the lineshape  $\lambda_{\perp}(\nu, \nu_a)$  for a selected ALP Compton frequency  $\nu_a$ , scaling it with signal power  $P_{\perp}(g_{\text{ap}})$  for a chosen coupling strength  $g_{\text{ap}}$  according to Eq. (B6), and then adding (“injecting”) the generated signal on top of a PSD spectrum obtained from the measurements. If many spectra over the same frequency range are being averaged during data analysis, the expected ALP signal would be sufficiently described by the time-averaged lineshape  $\lambda_{\perp}(\nu, \nu_a)$ . In our case, however, we look for signals in a single spectrum for each scan step. The amplitude of the ALP field at any frequency is a stochastic variable with values drawn from a Rayleigh distribution. The power that the ALP signal deposits in a single frequency bin of a PSD spectrum would be proportional to the square of its amplitude, and

is therefore drawn from an exponential distribution [28]. To account for this stochasticity, we performed a bin-wise random scaling of  $\lambda_{\perp}(\nu, \nu_a)$ , where the PSD values of the ALP signal are multiplied by numbers drawn from an exponential distribution with unitary mean. The “smooth” lineshape,  $\lambda_{\perp}(\nu, \nu_a)$ , would arise as the expectation value of the random-scaled ALP signal.

### Appendix C: Data analysis efficiency

A schematic overview of the data analysis strategy reported in this work can be found in Fig. 7.

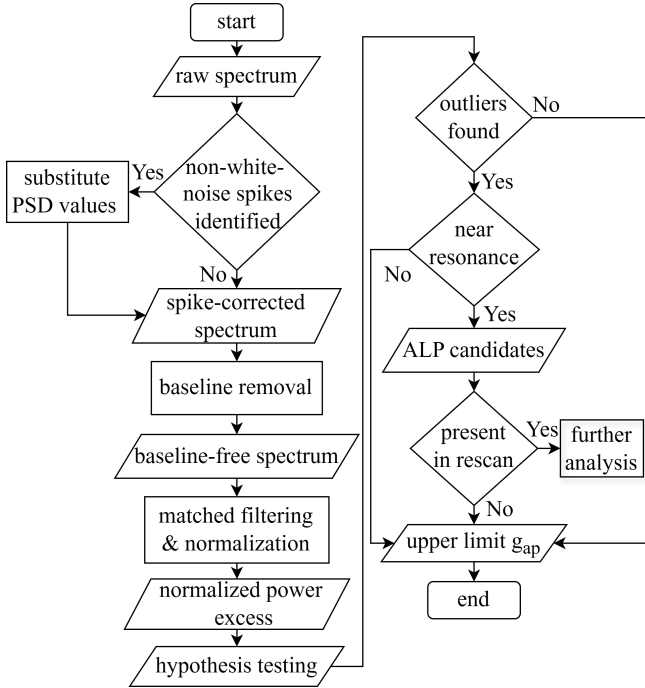


FIG. 7. Schematic of the data-analysis procedure. Non-white-noise-spike identification steps: (i) Obtain the histogram of the residual spectrum (difference between raw spectrum and narrow SG-filter output). (ii) Calculate threshold from a  $\chi^2_2$  fit to the histogram. Baseline removal: subtraction of and division by the broad-SG-filter output (baseline). Matched filtering: convolution of PSD with the ALP lineshape  $\lambda_{\perp}(\nu, \nu_a)$ . Hypothesis testing: identification of outliers from the rescan threshold for an ALP signal at the  $5\sigma$  level. ALP candidates: outliers within a window of  $\pm 5$  NMR linewidths around the Larmor frequency  $\nu_L$ .

#### 1. Data “sanity” check

We injected artificial ALP signals after baseline removal. The recovery of signals injected after baseline removal serves as a useful check, demonstrating our ability to recover signals from an ideal spectrum with a flat baseline. In Section C 2, we examine how baseline re-

moval affects the signal recovery and consider the overall efficiency of the data analysis.

We injected 20 different ALP signals with gradient couplings  $0.001 \text{ GeV}^{-1} < g_{a\text{NN}} < 0.1 \text{ GeV}^{-1}$  into a raw PSD spectrum generated from data taken in one of the scan steps. All artificial ALP signals were introduced at Compton frequencies randomly chosen from the analysis window. Injections and subsequent data analyses were carried out individually so that each spectrum used to test signal recovery only contained a single synthetic ALP signal. Figure 8 (a) showcases one synthetic ALP signal

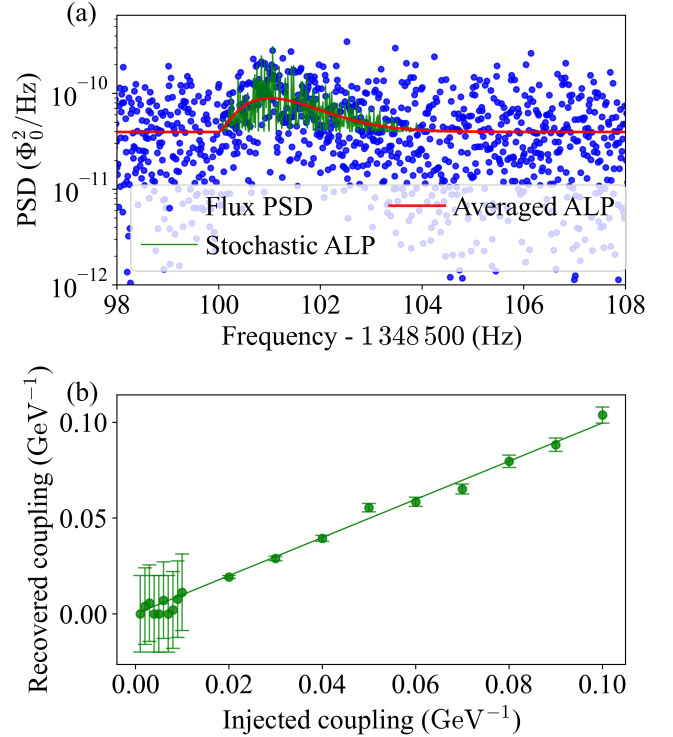


FIG. 8. (a) Zoomed-in view of the spectrum of one of the scan steps of the main scan. The PSD values are plotted in blue. Shown in red is the time-averaged signal lineshape  $\lambda_{\perp}(\nu, \nu_a)$  of one of the injected ALP signals, shown in green is  $\lambda_{\perp}(\nu, \nu_a)$  after random scaling with values drawn from an exponential distribution. (b) Gradient coupling constants recovered from 20 ALP signals, injected at random frequencies after baseline removal had been performed. Plotted are the signal power values of the matched filtered PSD at the ALP Compton frequencies converted into gradient coupling. Note that for couplings below the setup sensitivity, we indicate the uncertainty of the recovered value with the  $5\sigma$  sensitivity interval.

injected at a Compton frequency of  $\nu_a = 1\,348\,600 \text{ Hz}$ , with a gradient coupling of  $g_{\text{ap}} = 5 \times 10^{-2} \text{ GeV}^{-1}$ . This injected ALP signal is recovered by data analysis with a coupling of  $4.8 \times 10^{-2} \text{ GeV}^{-1}$  with an uncertainty of a few percent. The recovered coupling constants of all injected ALP signals are plotted in Fig. 8 (b). For the flat baseline case, an agreement between the injected and recovered coupling is expected, and in fact, we found a

linear relation with a slope of 0.999(7).

## 2. Effects of baseline removal

The effect of baseline removal depends on the shape of the baseline and, in our case, on the chosen window length of the SG filter. The SG filter used to obtain the baseline may accidentally fit potential ALP signal peaks as noise. When the filter window is sufficiently large, this can produce a significant shift in the NPE distribution obtained after filtering, compared to a scenario without baseline removal. This shift in NPE leads to a degradation of accuracy in recovering the signal coupling strength from NPE, which needs to be taken into account when evaluating the efficiency of the data analysis. We define the signal recovery efficiency including baseline removal,  $\eta_{\text{rec}}$ , as follows:

$$\eta_{\text{rec}} = \frac{e_{\text{rec}} - \langle e_{\text{off}} \rangle}{e_0}. \quad (\text{C1})$$

Here,  $e_{\text{rec}}$ ,  $e_0$ , and  $\langle e_{\text{off}} \rangle$  are the average NPE values at the frequency of an ALP signal with SG filter, without SG filter, and the offset due to the SG filter, respectively.

To compute the average efficiency, we used the baselines obtained via broad-SG filtering from ten of the PSD spectra. For each of these baselines, we generated 1000 sets of random noise data following a  $\chi^2$  distribution with two degrees of freedom and with the mean value adjusted to zero. These data sets simulate baseline-free, normalized spectra containing purely white noise (and are referred to as pure-noise spectra). An artificial ALP signal was injected into all data sets, with a coupling strength adjusted to ensure a  $5\text{-}\sigma$  significance in the absence of a baseline. Then, PSDs with non-flat baselines were simulated by combining the pure-noise data sets with the baselines from the measurements, as  $\text{baseline} \times (1 + \text{noise})$ . Both sets of PSDs, with and without baseline, underwent the analysis procedure to obtain their NPE. Finally, we constructed the histogram of NPE values recovered in the bin containing the frequency of the injected ALP across all simulated PSDs. Similarly, the distribution of NPE values in the absence of an ALP signal was collected from a frequency bin more than five ALP linewidths remote from the ALP frequency. Figure 9 depicts the NPE histograms for these scenarios: flat baseline, obtained from the pure-noise spectra, and non-flat baseline, obtained from the noise spectra combined with real baselines; with and without ALP signal for both cases. For a flat baseline [Fig. 9(a)], the NPE values recovered from the ALP signal bin (red) are distributed around a mean of  $e_0 = 5.0$ , consistent with the signal-to-noise ratio of the injected signal. In contrast, for spectra where the SG filter has removed a non-flat baseline [Fig. 9(b)], the distribution of ALP signal NPEs is shifted, with a mean of  $e_{\text{rec}} = 4.36$ . The average offset due to the effect of the filter,  $\langle e_{\text{off}} \rangle$ , is obtained from the difference between the no-ALP NPE histograms with

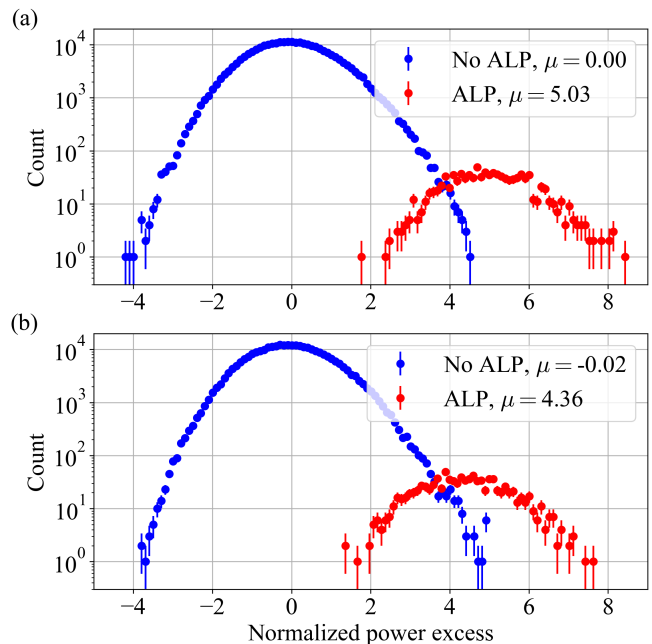


FIG. 9. Histogram of normalized power excess (pull distribution) with ALP (red) and without ALP (blue). (a) Flat baseline. (b) With real baseline and SG filter. Here,  $\mu$  refers to the mean of a histogram.

and without baseline. We arrive at an average recovery efficiency  $\eta_{\text{rec}} = 88.2(4.6)\%$ . In terms of signal coupling strength, the efficiency is  $\sqrt{\eta_{\text{rec}}} = 93.9(2.5)\%$  and has been taken into account in the calculation of the sensitivity limits.

## 3. Finding the rescan threshold

Previously, we obtained the expected distribution of NPE values depending on the presence of an ALP signal, through Monte-Carlo (MC) simulations. To determine whether the NPE of each frequency bin of a spectrum obtained from the experiment is likely to be a signal from ALPs or a statistical fluctuation, we performed a hypothesis test.

In the simulation, we assumed an ALP with a coupling strength corresponding to  $5\sigma$ . This signal was used as the null hypothesis. From it, we found the NPE providing a 95% confidence level. We calculated the empirical cumulative distribution function (CDF) using the histogram of NPE values at the ALP signal frequency bin obtained through MC simulations for the case of a flat baseline, i.e., the ideal case without using an SG filter. Figure 10 shows the empirical CDF obtained from MC simulation. The threshold value at the 95% confidence interval limit was found to be  $\Theta_{\text{RE}} = 3.43$ . In the actual experiment, frequency components that yielded a NPE greater than this were considered signal candidates or outliers, depending on whether they were on resonance

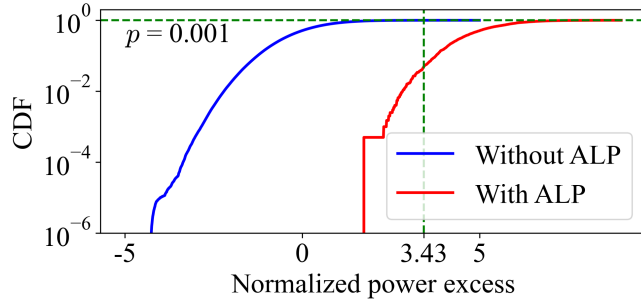


FIG. 10. The empirical CDF obtained from the NPE distribution of spectra with a flat baseline [refer to Fig. 9(a)]. The vertical dashed line represents the threshold for rescan,  $\Theta_{RE}$ , corresponding to the null hypothesis of a  $5\sigma$  ALP detection at the 95% confidence level. The p-value corresponding to the threshold (horizontal dashed line) is approximately 0.001.

or not. Outliers from the main scan were compared with scans A and B in order to determine if they were signals from statistical fluctuations.

- [1] F. Zwicky *et al.*, The redshift of extragalactic nebulae, *Helv. Phys. Acta* **6**, 138 (1933).
- [2] F. Zwicky, On the masses of nebulae and of clusters of nebulae, in *A Source Book in Astronomy and Astrophysics, 1900–1975* (Harvard University Press, 1979) pp. 729–737.
- [3] V. C. Rubin and W. K. Ford Jr, Rotation of the andromeda nebula from a spectroscopic survey of emission regions, *Astrophysical Journal*, vol. 159, p. 379 **159**, 379 (1970).
- [4] P. Ade, N. Aghanim, Y. Akrami, P. Aluri, M. Arnaud, M. Ashdown, J. Aumont, C. Baccigalupi, A. Banday, R. Barreiro, *et al.*, Planck 2015 results-XVI. Isotropy and statistics of the CMB, *Astronomy & Astrophysics* **594**, A16 (2016).
- [5] M. Bartelmann, Gravitational lensing, *Classical and Quantum Gravity* **27**, 233001 (2010).
- [6] D. Clowe, M. Bradač, A. H. Gonzalez, M. Markevitch, S. W. Randall, C. Jones, and D. Zaritsky, A direct empirical proof of the existence of dark matter, *The Astrophysical Journal* **648**, L109–L113 (2006).
- [7] D. Harvey, R. Massey, T. Kitching, A. Taylor, and E. Tittley, The nongravitational interactions of dark matter in colliding galaxy clusters, *Science* **347**, 1462–1465 (2015).
- [8] K. Jedamzik and M. Pospelov, Big bang nucleosynthesis and particle dark matter, *New Journal of Physics* **11**, 105028 (2009).
- [9] P. W. Graham, I. G. Irastorza, S. K. Lamoreaux, A. Lindner, and K. A. van Bibber, Experimental searches for the axion and axion-like particles, *Annual Review of Nuclear and Particle Science* **65**, 485 (2015).
- [10] F. Chadha-Day, J. Ellis, and D. J. E. Marsh, Axion dark matter: What is it and why now? (2022), arXiv:2105.01406 [hep-ph].
- [11] D. F. Jackson Kimball and K. Van Bibber, *The search for ultralight bosonic dark matter* (Springer Nature, 2023).
- [12] P. W. Graham and A. Scherlis, Stochastic axion scenario, *Phys. Rev. D* **98**, 035017 (2018).
- [13] J. Preskill, M. B. Wise, and F. Wilczek, Cosmology of the invisible axion, *Physics Letters B* **120**, 127 (1983).
- [14] L. F. Abbott and P. Sikivie, A Cosmological Bound on the Invisible Axion, *Phys. Lett. B* **120**, 133 (1983).
- [15] M. Dine and W. Fischler, The not-so-harmless axion, *Physics Letters B* **120**, 137 (1983).
- [16] P. Svrcek and E. Witten, Axions in string theory, *Journal of High Energy Physics* **2006**, 051 (2006).
- [17] R. D. Peccei and H. R. Quinn, CP Conservation in the Presence of Pseudoparticles, *Phys. Rev. Lett.* **38**, 1440 (1977).
- [18] R. D. Peccei and H. R. Quinn, Constraints imposed by CP conservation in the presence of pseudoparticles, *Phys. Rev. D* **16**, 1791 (1977).
- [19] L. Bergström, P. Ullio, and J. H. Buckley, Observability of  $\gamma$  rays from dark matter neutralino annihilations in the Milky Way halo, *Astroparticle Physics* **9**, 137 (1998).
- [20] G. Jungman, M. Kamionkowski, and K. Griest, Supersymmetric dark matter, *Physics Reports* **267**, 195 (1992).
- [21] Y. Sofue and V. Rubin, Rotation Curves of Spiral Galaxies, *Annual Review of Astronomy and Astrophysics* **39**, 137 (2001).
- [22] J. W. Foster, N. L. Rodd, and B. R. Safdi, Revealing the dark matter halo with axion direct detection, *Phys. Rev. D* **97**, 123006 (2018).
- [23] M. Lisanti, M. Moschella, and W. Terrano, Stochastic properties of ultralight scalar field gradients, *Phys. Rev. D* **104**, 055037 (2021).
- [24] D. Y. Cheong, N. L. Rodd, and L.-T. Wang, Quantum description of wave dark matter, *Phys. Rev. D* **111**, 015028 (2025).
- [25] J. R. Primack, D. Seckel, and B. Sadoulet, Detection of cosmic dark matter, *Annual Review of Nuclear and Particle Science* **38**, 751 (1988).
- [26] D. F. Jackson Kimball, S. Afach, D. Aybas, J. W. Blanchard, D. Budker, G. Centers, M. Engler, N. L. Figueroa, A. Garcon, P. W. Graham, H. Luo, S. Rajendran, M. G. Sendra, A. O. Sushkov, T. Wang, A. Wickenbrock, A. Wilzewski, and T. Wu, Overview of the cosmic axion spin precession experiment (CASPER), in *Microwave Cavities and Detectors for Axion Research*, edited by G. Carosi and G. Rybka (Springer International Publishing, Cham, 2020) pp. 105–121.
- [27] N. W. Evans, C. A. J. O’Hare, and C. McCabe, Refinement of the standard halo model for dark matter searches in light of the Gaia Sausage, *Phys. Rev. D* **99**, 023012 (2019).
- [28] A. V. Gramolin, A. Wickenbrock, D. Aybas, H. Bekker, D. Budker, G. P. Centers, N. L. Figueroa, D. F. Jackson Kimball, and A. O. Sushkov, Spectral signatures of axionlike dark matter, *Phys. Rev. D* **105**, 035029 (2022).
- [29] Schive, Hsi-Yu, Chiueh, Tzihong, and Broadhurst, Tom, Cosmic structure as the quantum interference of a coherent dark wave, *Nature Physics* **10**, 496 (2014).
- [30] G. P. Centers, J. W. Blanchard, J. Conrad, N. L. Figueroa, A. Garcon, A. V. Gramolin, D. F. J. Kimball, M. Lawson, B. Pelssers, J. A. Smiga, A. O. Sushkov, A. Wickenbrock, D. Budker, and A. Derevianko, Stochastic fluctuations of bosonic dark matter, *Nature Communications* **12**, 7321 (2021).
- [31] J. L. Ouellet, C. P. Salemi, J. W. Foster, R. Henning, Z. Bogorad, J. M. Conrad, J. A. Formaggio, Y. Kahn, J. Minervini, A. Radovinsky, *et al.*, First results from ABRACADABRA-10 cm: a search for sub- $\mu$  eV axion dark matter, *Physical review letters* **122**, 121802 (2019).
- [32] N. Du, N. Force, R. Khatiwada, E. Lentz, R. Ottens, L. Rosenberg, G. Rybka, G. Carosi, N. Woollett, D. Bowring, *et al.*, Search for invisible axion dark matter with the axion dark matter experiment, *Physical review letters* **120**, 151301 (2018).
- [33] A. J. Millar, S. M. Anlage, R. Balafendiev, P. Belov, K. van Bibber, J. Conrad, M. Demarteau, A. Droster, K. Dunne, A. G. Rosso, J. E. Gudmundsson, H. Jackson, G. Kaur, T. Klaesson, N. Kowitz, M. Lawson, A. Leder, A. Miyazaki, S. Morampudi, H. V. Peiris, H. S. Røising, G. Singh, D. Sun, J. H. Thomas, F. Wilczek, S. Withington, M. Wooten, J. Dilling, M. Febbraro, S. Knirck, and C. Marvinnay (Endorsers), Searching for dark matter with plasma haloscopes, *Phys. Rev. D* **107**, 055013 (2023).
- [34] B. Aja, S. A. Cuendis, I. Arregui, E. Artal, R. B. Barreiro, F. J. Casas, M. C. de Ory, A. Díaz-Morcillo, L. de la Fuente, J. D. Gallego, *et al.*, The canfranc axion detection experiment (CADEx): Search for axions at 90 GHz

- with kinetic inductance detectors, *Journal of Cosmology and Astroparticle Physics* **2022** (11), 044.
- [35] S. Ahn, J. Kim, B. I. Ivanov, O. Kwon, H. Byun, A. F. van Loo, S. Park, J. Jeong, S. Lee, J. Kim, i. m. c. b. u. Kutlu, A. K. Yi, Y. Nakamura, S. Oh, D. Ahn, S. Bae, H. Choi, J. Choi, Y. Chong, W. Chung, V. Gkika, J. E. Kim, Y. Kim, B. R. Ko, L. Miceli, D. Lee, J. Lee, K. W. Lee, M. Lee, A. Matlashov, P. Parashar, T. Seong, Y. C. Shin, S. V. Uchaikin, S. Youn, and Y. K. Semertzidis, Extensive Search for Axion Dark Matter over 1 GHz with CAPP'S Main Axion Experiment, *Phys. Rev. X* **14**, 031023 (2024).
- [36] L. Brouwer, S. Chaudhuri, H.-M. Cho, J. Corbin, W. Craddock, C. Dawson, A. Droster, J. Foster, J. Fry, P. Graham, *et al.*, Projected sensitivity of DMRadio-m 3: A search for the QCD axion below  $1 \mu\text{eV}$ , *Physical Review D* **106**, 103008 (2022).
- [37] D. Alesini, D. Babusci, P. Beltrame, F. Bossi, P. Ciambrone, A. D'Elia, D. Di Gioacchino, G. Di Pirro, B. Döbrich, P. Falferi, *et al.*, The future search for low-frequency axions and new physics with the FLASH resonant cavity experiment at Frascati National Laboratories, *Physics of the Dark Universe* **42**, 101370 (2023).
- [38] L. Zhong, S. Al Kenany, K. Backes, B. Brubaker, S. Cahn, G. Carosi, Y. Gurevich, W. Kindel, S. Lamoreaux, K. Lehnert, *et al.*, Results from phase 1 of the HAYSTAC microwave cavity axion experiment, *Physical Review D* **97**, 092001 (2018).
- [39] B. A. dos Santos Garcia, D. Bergermann, A. Caldwell, V. Dabhi, C. Diaconu, J. Diehl, G. Dvali, J. Egge, E. Garutti, S. Heyminck, F. Hubaut, A. Ivanov, J. Jochum, S. Knirck, M. Kramer, D. Kreikemeyer-Lorenzo, C. Krieger, C. Lee, D. Leppla-Weber, X. Li, A. Lindner, B. Majorovits, J. P. A. Maldonado, A. Martini, A. Miyazaki, E. Öz, P. Pralavorio, G. Raffelt, J. Redondo, A. Ringwald, J. Schaffran, A. Schmidt, F. Steffen, C. Strandhagen, I. Usherov, H. Wang, and G. Wieching, First search for axion dark matter with a MADMAX prototype (2024), arXiv:2409.11777 [hep-ex].
- [40] A. P. Quiskamp, G. Flower, S. Samuels, B. T. McAllister, P. Altin, E. N. Ivanov, M. Goryachev, and M. E. Tobar, Near-quantum limited axion dark matter search with the ORGAN experiment around  $26 \mu\text{eV}$ , arXiv preprint arXiv:2407.18586 (2024).
- [41] A. Rettaroli, D. Alesini, D. Babusci, C. Braggio, G. Carugno, D. D'Agostino, A. D'Elia, D. Di Gioacchino, R. Di Vora, P. Falferi, U. Gambardella, A. Gardikiotis, C. Gatti, C. Ligi, A. Lombardi, G. Maccarrone, A. Ortolan, G. Ruoso, S. Tocci, and G. Vidali (QUAX Collaboration), Search for axion dark matter with the QUAX-LNF tunable haloscope, *Phys. Rev. D* **110**, 022008 (2024).
- [42] A. V. Gramolin, D. Aybas, D. Johnson, J. Adam, and A. O. Sushkov, Search for axion-like dark matter with ferromagnets, *Nature Physics* **17**, 79 (2021).
- [43] D. Gavilan-Martin, G. Lukaszewicz, M. Padniuk, E. Klinger, M. Smolis, N. L. Figueroa, D. F. J. Kimball, A. O. Sushkov, S. Pustelny, D. Budker, *et al.*, Searching for dark matter with a 1000 km baseline interferometer, arXiv preprint arXiv:2408.02668 (2024).
- [44] I. M. Bloch, G. Ronen, R. Shaham, O. Katz, T. Volansky, and O. Katz, New constraints on axion-like dark matter using a Floquet quantum detector, *Science Advances* **8**, eabl8919 (2022), <https://www.science.org/doi/pdf/10.1126/sciadv.abl8919>.
- [45] T. Wu, J. W. Blanchard, G. P. Centers, N. L. Figueroa, A. Garcon, P. W. Graham, D. F. J. Kimball, S. Rajendran, Y. V. Stadnik, A. O. Sushkov, *et al.*, Search for axionlike dark matter with a liquid-state nuclear spin comagnetometer, *Physical review letters* **122**, 191302 (2019).
- [46] C. Abel, N. J. Ayres, G. Ban, G. Bison, K. Bodek, V. Bondar, E. Chanel, C. Crawford, M. Daum, B. Dechenaux, *et al.*, Search for ultralight axion dark matter in a side-band analysis of a  $^{199}\text{Hg}$  free-spin precession signal, *SciPost Physics* **15**, 058 (2023).
- [47] S. Karanth, E. J. Stephenson, S. P. Chang, V. Hejny, S. Park, J. Pretz, Y. K. Semertzidis, A. Wirzba, A. Wrońska, F. Abusaif, *et al.*, First search for axion-like particles in a storage ring using a polarized deuteron beam, *Physical Review X* **13**, 031004 (2023).
- [48] J. Lee, M. Lisanti, W. A. Terrano, and M. Romalis, Laboratory constraints on the neutron-spin coupling of fev-scale axions, *Physical Review X* **13**, 011050 (2023).
- [49] F. Capozzi, B. Dutta, G. Gurung, W. Jang, I. M. Shoemaker, A. Thompson, and J. Yu, New constraints on ALP couplings to electrons and photons from ArgoNeUT and the MiniBooNE beam dump, *Physical Review D* **108**, 075019 (2023).
- [50] D. Budker, P. W. Graham, M. Ledbetter, S. Rajendran, and A. O. Sushkov, Proposal for a Cosmic Axion Spin Precession Experiment (CASPER), *Phys. Rev. X* **4**, 021030 (2014).
- [51] T. Wang, D. F. J. Kimball, A. O. Sushkov, D. Aybas, J. W. Blanchard, G. Centers, S. R. O'Kelley, A. Wickenbrock, J. Fang, and D. Budker, Application of spin-exchange relaxation-free magnetometry to the cosmic axion spin precession experiment, *Physics of the dark universe* **19**, 27 (2018).
- [52] D. Aybas, J. Adam, E. Blumenthal, A. V. Gramolin, D. Johnson, A. Kleyheeg, S. Afach, J. W. Blanchard, G. P. Centers, A. Garcon, *et al.*, Search for axionlike dark matter using solid-state nuclear magnetic resonance, *Physical Review Letters* **126**, 141802 (2021).
- [53] A. Garcon, J. W. Blanchard, G. P. Centers, N. L. Figueroa, P. W. Graham, D. F. J. Kimball, S. Rajendran, A. O. Sushkov, Y. V. Stadnik, A. Wickenbrock, T. Wu, and D. Budker, Constraints on bosonic dark matter from ultralow-field nuclear magnetic resonance, *Science Advances* **5**, eaax4539 (2019).
- [54] A. Garcon, D. Aybas, J. W. Blanchard, G. Centers, N. L. Figueroa, P. W. Graham, D. F. J. Kimball, S. Rajendran, M. G. Sendra, A. O. Sushkov, *et al.*, The Cosmic Axion Spin Precession Experiment (CASPER): a dark-matter search with nuclear magnetic resonance, *Quantum Science and Technology* **3**, 014008 (2017).
- [55] J. Walter, H. Bekker, J. Blanchard, D. Budker, N. L. Figueroa, A. Wickenbrock, Y. Zhang, and P. Zhou, Fast shimming algorithm based on bayesian optimization for magnetic resonance based dark matter search, *Annalen der Physik* **536**, 2300258 (2024).
- [56] Y. Zhang, D. A. Turturk, H. Bekker, D. Budker, D. F. J. Kimball, A. O. Sushkov, and A. Wickenbrock, Frequency-Scanning Considerations in Axionlike Dark Matter Spin-Precession Experiments, *Annalen der Physik* **536**, 2300223 (2024).
- [57] J. Clarke and A. I. Braginski, *The SQUID handbook: Applications of SQUIDs and SQUID systems* (John Wiley

- & Sons, 2006).
- [58] H. Y. Carr and E. M. Purcell, Effects of Diffusion on Free Precession in Nuclear Magnetic Resonance Experiments, *Phys. Rev.* **94**, 630 (1954).
- [59] B. M. Brubaker, L. Zhong, S. K. Lamoreaux, K. W. Lehnert, and K. A. van Bibber, HAYSTAC axion search analysis procedure, *Physical Review D* **96**, 10.1103/physrevd.96.123008 (2017).
- [60] A. Gramolin, D. Aybas, D. Johnson, J. Adam, and A. Sushkov, Search for Halo Axions with Ferromagnetic Toroids (SHAFT Experiment), in *APS April Meeting Abstracts*, Vol. 2021 (2021) p. L19.008.
- [61] A. Arza, A. Kryemadhi, and K. Zioutas, Searching for axion streams with the echo method, *Phys. Rev. D* **108**, 083001 (2023), arXiv:2212.10905 [hep-ph].
- [62] C. A. J. O'Hare, G. Pierobon, and J. Redondo, Axion Minicluster Streams in the Solar Neighborhood, *Phys. Rev. Lett.* **133**, 081001 (2024).
- [63] J. De Miguel, A. Kryemadhi, and K. Zioutas (On behalf of the DALI Collaboration), DALI sensitivity to streaming axion dark matter, *Phys. Rev. D* **111**, 023016 (2025).
- [64] A. Savitzky and M. J. E. Golay, Smoothing and differentiation of data by simplified least squares procedures., *Analytical Chemistry* **36**, 1627 (1964), <https://doi.org/10.1021/ac60214a047>.
- [65] D. A. Freedman and P. Diaconis, On the histogram as a density estimator:L2 theory, *Zeitschrift für Wahrscheinlichkeitstheorie und Verwandte Gebiete* **57**, 453 (1981).
- [66] J. Eills, D. Budker, S. Cavagnero, E. Y. Chekmenev, S. J. Elliott, S. Jannin, A. Lesage, J. Matysik, T. Meersmann, T. Prisner, J. A. Reimer, H. Yang, and I. V. Koptug, Spin Hyperpolarization in Modern Magnetic Resonance, *Chemical Reviews* **123**, 1417 (2023), PMID: 36701528, <https://doi.org/10.1021/acs.chemrev.2c00534>.
- [67] G. G. Raffelt, Particle physics from stars, *Annual Review of Nuclear and Particle Science* **49**, 163 (1999).
- [68] A. Abragam and H. Y. Carr, The principles of nuclear magnetism, *Physics Today* **14**, 56 (1961).